Rapid Communications

Optically pumped dynamic nuclear hyperpolarization in ^{13}C-enriched diamond

Anna J. Parker, Keunhong Jeong, Claudia E. Avalos, Birgit J. M. Hausmann, Christophoros C. Vassiliou, Alexander Pines, and Jonathan P. King*

Department of Chemistry, University of California, Berkeley, California 94720, USA
and Materials Sciences Division, Lawrence Berkeley National Laboratory, Berkeley, California 94720, USA

(Received 26 July 2017; revised manuscript received 24 September 2017; published 30 July 2019)

We investigate nuclear spin hyperpolarization from optically polarized nitrogen vacancy centers in isotopically enriched diamonds with ^{13}C concentrations up to 100%. ^{13}C enrichment leads to a nitrogen vacancy electron spin resonance with a complex hyperfine structure and dynamic nuclear polarization enhancement profile. We show that strongly coupled ^{13}C spins in the first shell surrounding a nitrogen vacancy center generate resolved hyperfine splittings, but do not act as an intermediary in the transfer of hyperpolarization of bulk nuclear spins. High levels of ^{13}C enrichment are desirable to increase the efficiency of hyperpolarization for magnetic resonance signal enhancement, imaging contrast agents, and as a platform for quantum sensing and many-body physics.

DOI: 10.1103/PhysRevB.100.041203

The last decade has witnessed rapid strides in the development of quantum technologies based on atomlike defect centers in solids [1,2], such as the negatively charged nitrogen vacancy (NV^-) center [3]. The NV^- is a system of six localized electrons in diamond with a total spin of 1, whose properties have drawn attention from various scientific fields. For example, optical initialization of the NV^- spin state [4], long electron spin coherence times exceeding 1 ms [5,6], and optical spin state readout [7] have made the defect a model platform for quantum information processing [8–10], simulation [11,12], and metrology [13–15].

Nearly all of these technologies require knowledge of and capitalization upon the interactions of the NV^- center with nearby nuclear spins both in and external to the diamond. Tuning the ^{13}C concentration by isotopic growth techniques [16] enables a variety of quantum technology schemes. For instance, in the limit of low nuclear concentrations ($\leqslant$1%), NV^--^{13}C pairs can form quantum registers [17–19] with increased sensing resolution [20,21] and sensitivity [22]. At slightly higher concentrations ($\sim$10%), a single NV^- center can be coupled to a number of ^{13}C nuclei to form the node of a quantum information processor, allowing indirect fast actuation and universal quantum control on the nuclear spins via the electronic qubit [23,24]. At high concentrations beyond 50% and approaching 100% where internuclear couplings become significant, hybridized nuclear spin states enable decoherence protected subspaces [25] where classical information can stored. This also forms a versatile system to study various condensed matter phenomena in the strongly dipolar coupled quantum networks [26], including notions of quantum transport [27], localization and criticality [28,29], and Floquet many-body phases [30–32].

Additionally, optically polarized electron spin systems such as NV^- or the divacancy defect in silicon carbide [33] provide an exciting opportunity for long-standing nuclear magnetic resonance (NMR) and magnetic resonance imaging (MRI) technologies. While NMR and MRI are indispensable tools in the fields of chemistry, biology, engineering, and medicine, their sensitivity relies on nuclear spin initialization (i.e., polarization), which at best reaches 10^{-4} at room temperature. In stark contrast to the weak magnetization of nuclear spins, optical pumping hyperpolarizes the NV^- spin state beyond thermal equilibrium at arbitrary temperature and over a wide range of magnetic fields [34]. As a result, a number of schemes for creating nuclear spin hyperpolarization have been reported in the recent literature based on applying traditional dynamic nuclear polarization (DNP) methods [35] to either single NV^- centers [36] or NV^- ensembles [37–44]. These schemes propose the use of hyperpolarized ^{13}C nuclei in diamond for use as MRI contrast agents [45] as well as a platform for polarization transfer to external nuclei [43] for enhanced magnetic resonance signals from arbitrary samples. In these cases, the low natural abundance (1.1%) of ^{13}C nuclear spins limits the efficiency of hyperpolarization and it is desirable to work with ^{13}C-enriched materials.

Here, we report NV^- DNP hyperpolarization of ^{13}C-enriched diamonds. Our methods result in significant ^{13}C bulk polarizations approaching 0.1% at approximately 0.5 T in a variety of samples, an enhancement of three orders of magnitude over thermal polarization. We show how isotopic enrichment imparts a complex structure to the electron spin resonance (ESR) spectrum and corresponding DNP spectrum. The DNP spectra lend insight to the mechanism of polarization transfer, illustrating that NV^- centers and the first shell of ^{13}C spins behave as a strongly coupled system that transfers polarization directly to weakly coupled nuclear spins. These findings open the path to their use as efficient external polarizing agents, and for applications in quantum technologies.

In this Rapid Communication, we employ continuous-wave (cw) DNP to hyperpolarize ^{13}C nuclei in a set of single-crystal diamonds at a magnetic field of approximately 472 mT with the NV^- crystal axis aligned along the magnetic field. A

*jpking@berkeley.edu

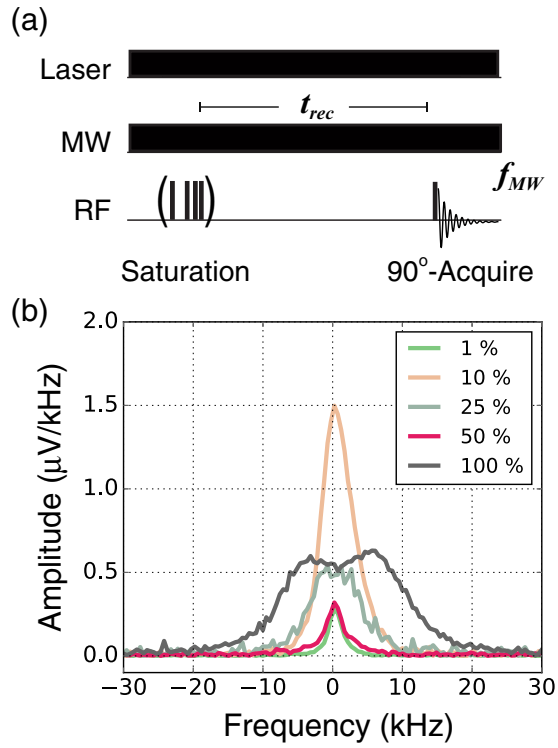

FIG. 1. cw-DNP with NV^- centers. A schematic for the cw-DNP experiment is shown in (a). The experiment begins by saturating the spins with a series of 90° pulses, each followed by a dephasing period, which destroys any residual ^{13}C polarization and ensures the same initial nuclear polarization for each experiment. The ^{13}C polarization then builds under continuous optical and microwave excitation. The microwave frequency f_{MW} is swept to find the optimum frequency. After the ^{13}C nuclear polarization builds during a recovery time t_{rec}, a single 90° pulse is applied and the NMR signal is acquired. The spectra of the hyperpolarized ^{13}C NMR resulting from optimizing f_{MW} and the polarization buildup time are shown in (b) for samples with a natural abundance (1.1%) ^{13}C and 10%, 25%, 50%, and 100% ^{13}C enrichment.

schematic of the DNP pulse sequence is given in Fig. 1(a). Each experiment begins with a set of 90° pulses, which acts to destroy any residual ^{13}C polarization. This ensures the same initial nuclear polarization for each experiment. The ^{13}C polarization then builds under continuous optical and microwave irradiation for a recovery time t_{rec}. The laser optically pumps the NV^- center to continually initialize its spin state, while microwave irradiation has the effect of transferring spin polarization between NV^- and ^{13}C spins, thus hyperpolarizing the ^{13}C spins and producing enhanced NMR signals. The hyperpolarized ^{13}C NMR spectra of each sample are shown in Fig. 1(b), where the effects of the nuclear dipole-dipole couplings are apparent in the doublet spectrum of the 100% ^{13}C diamond.

In a field of 472 mT, NV^- spin transitions are observed at approximately 16.1 and 10.3 GHz [Fig. 2(a)]. Here, we focus on the higher-frequency transition. We read out the NV^- spin state via optically detected magnetic resonance (ODMR), where the NV^- fluorescence intensity is monitored while sweeping the microwave frequency. Because the $m_s = \pm 1$ states are more likely to relax via intersystem crossing to the ground electronic state, resonant microwave excitation produces a detectable change in the NV^- fluorescence intensity [3]. ^{13}C spins within the first shell of nuclei, those directly adjacent to the NV^- defect, are strongly coupled to the NV^- spin and give a resolved hyperfine structure (Fig. 2). In a ^{13}C-enriched sample, the three nearest-neighbor sites are occupied by zero, one, two, or three ^{13}C nuclei with the balance occupied by spinless ^{12}C. The ODMR spectrum is therefore a superposition of four distinct patterns of hyperfine splittings with relative intensities determined by the degree of enrichment. The pattern of hyperfine splittings in Fig. 2 is consistent with the known ^{13}C-NV^- hyperfine tensor for first-shell nuclear spins [47].

The DNP process involves driving NV^- spin transitions to transfer polarization to nearby ^{13}C spins. The microscopic mechanism of DNP depends on the degree of homogeneous and inhomogeneous broadening of the electron spin resonance as well as its width relative to the nuclear Larmor frequency ω_n [35]. In our experiments the differential solid effect, cross effect, and thermal mixing mechanisms of DNP all potentially contribute, and are difficult to distinguish. In the natural abundance sample the ESR linewidth is likely dominated by strain broadening and interactions with $P1$ centers, while for the enriched samples hyperfine coupling to ^{13}C dominates. While the solid effect mechanism is the simplest case involving a single electron and single nuclear spin, the cross effect and thermal mixing mechanisms involve two- or multielectron spin flips whose net energy is on the order of ω_n. Cross effect mechanisms tend to dominate in the limit of an inhomogeneously broadened electron spin resonance while thermal mixing dominates in the limit of a homogeneously broadened electron spin resonance [35,48]. Because our sample composition also varies in NV^-, $P1$ center, and ^{13}C concentration, it is likely the mechanism varies by sample.

Regardless of the local DNP mechanism, nuclear spin diffusion transports polarization to bulk ^{13}C spins that do not interact directly with the NV^- center. The nuclear spin diffusion constant D for ^{13}C in diamond with a natural isotopic abundance is known to be 6.7×10^{-15} cm^2/s [49]. We estimate D for the other samples using the following relation [50],

$$D = \frac{\Delta\nu_{dd} a^2}{30}. \quad (1)$$

Here, $\Delta\nu_{dd}$ is the linewidth due to nuclear dipole-dipole coupling, and a is the average separation between nuclear spins which may be estimated from concentration ρ by $a = \rho^{-1/3}$. Estimating $\Delta\nu_{dd}$ is straightforward only for the 100% ^{13}C sample, where the NMR linewidth is clearly dominated by nuclear dipole-dipole interactions rather than high concentrations of electron spins or magnetic field inhomogeneity, as may be the case for the other samples (see Fig. 1). As a result, we estimate $\Delta\nu_{dd}$ from the 100% ^{13}C sample from the square root of the second moment of the NMR line shape (8.26 kHz ± 0.09). The spin diffusion coefficient typically exhibits a square root dependence on concentration of nuclei for concentrations between 10% and 100% [50,51], and we use this relationship to estimate D for the remaining enriched

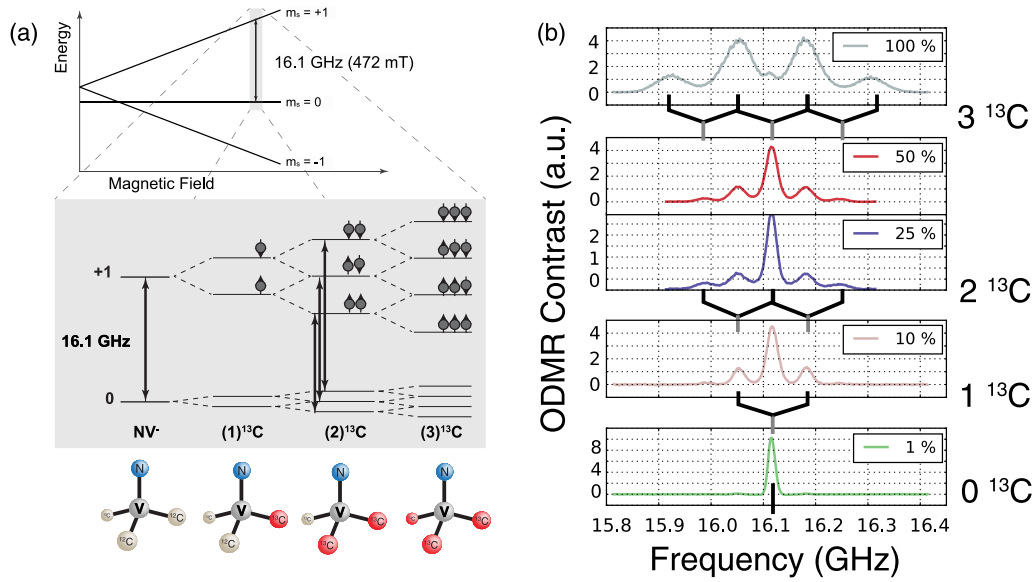

FIG. 2. The effect of ^{13}C enrichment on the energy level structure and ODMR spectroscopy of NV$^-$ centers. The energy level structure of the NV$^-$ as a function of magnetic field strength is shown in (a), where the magnetic field regime relevant to DNP experiments is highlighted and expanded. Here, we focus on the high-energy transition from the NV$^-$ $m_s = 0$ to $m_s = +1$ at 472 mT, which has a frequency of approximately 16.1 GHz. The strongest hyperfine interactions occur between the NV$^-$ and its first-shell ^{13}C nuclei, those directly adjacent to it. Occupation of the first-shell sites leads to a splitting in not only the NV$^-$ $m_s = \pm 1$ levels, but also the $m_s = 0$ due to the anisotropic component of the coupling. The magnified energy level diagram shows how the NV$^-$ spin states split into hyperfine states determined by the different possible combinations of nuclear spin, as one, two, and three carbons are added. Diagrams of the NV$^-$ as well as the occupation of the first-shell sites with ^{13}C nuclei are given below the energy level diagram. The branching in these energy levels corresponds directly to the structure seen in the ODMR spectra of diamonds with varying ^{13}C enrichment (b). A single line is observed for the $m_s = 0$ to $m_s = +1$ transition in the NV$^-$ spin state for a sample with a natural abundance (1.1%) of ^{13}C, whereas a sample with 100% ^{13}C enrichment exhibits a quartet for the same transition [46].

samples. The estimates are given in Table I along with estimates of the spin diffusion length L during polarization buildup time, calculated with the relation $L = \sqrt{DT_{\mathrm{DNP}}}$.

In general, the DNP intensity has an antisymmetric frequency dependence and is related to the intensity of the ODMR spectrum (Fig. 3), consistent with DNP mechanisms where the EPR spectrum is broader than the nuclear Larmor frequency. Interestingly, this trend holds for the satellite peaks induced by the strongly hyperfine-coupled ^{13}C spins in the first shell, indicating that direct driving of the strongly coupled hyperfine transition does not generate bulk polarization. This contrasts with NV$^-$ hyperpolarization near a level anticrossing where highly mixed electron-nuclear spin states result in hyperpolarization of first-shell ^{13}C which is then transported to bulk nuclear spins [38]. Here, the symmetric intensities of the hyperfine-induced DNP satellites and the derivative DNP patterns at each satellite transition indicate the polarization of the first-shell ^{13}C spins does not play a role in the bulk DNP, other than to induce a splitting of the NV$^-$ spectrum. Note that this does not mean the first-shell nuclei are not being polarized as well, as they are not observed in our experiments.

The level of maximum hyperpolarization is sample dependent due to the varied concentration of ^{13}C, NV$^-$ centers, and other paramagnetic defects that cause nuclear spin relaxation (see Table I). We note that ^{13}C enrichment may increase the rate of relaxation alongside increasing the polarization buildup rate, and in fact these rates may be closely linked. The steady-state polarization represents a balance of these processes [52]. The highest level of polarization was achieved in the natural abundance diamond, which has the highest NV$^-$ concentration while the highest total magnetization occurred in the 100% diamond We note that the maximum enhancement observed in the natural abundance sample (1264) is less than reported previously [43]. This may be due to a different sample with different defect concentrations and relaxation times, as well as a different experimental apparatus that may deliver microwave power less efficiently. We regard the present results as being more reliable because of the use of the diamond thermal signal itself as a calibration rather than an external standard [52]. The 100% ^{13}C diamond also exhibited the fastest buildup of hyperpolarization (Fig. 4), suggesting that the enhanced rate of nuclear spin diffusion more efficiently transports polarization to bulk nuclei. All other parameters being equal, we expect 100% ^{13}C diamonds to be optimum for MRI contrast and polarization transfer applications. We have shown that, despite the spectral complexity associated with multiple strong hyperfine couplings, hyperpolarization can be efficiently transferred to bulk nuclear spins. Furthermore, the control we demonstrate over bulk nuclear spin polarization in samples with a high nuclear spin concentration provide insight for and enable the development of quantum technologies employing strongly coupled spin systems.

This work was supported by the U.S. Department of Energy, Office of Science, Basic Energy Sciences under Contract

TABLE I. Summary of the polarization buildup time T_{DNP}, enhanced ^{13}C nuclear polarization (P_{enh}), and maximum DNP enhancement for each diamond sample as well as parameters useful for evaluating DNP mechanisms ($\Delta\nu_{NV}$, Δ_{DNP}), estimates of spin diffusion constants (D), and the spin diffusion length (L) during polarization buildup.

Sample	*D*1	*D*2	*D*3	*D*4	*D*5
[^{13}C] (%)	1	10	25	50	100
$\Delta\nu_{NV}$ (MHz)	17	26	23.5	27	52
T_{DNP} (s)	22.34 ± 0.06	59.55 ± 0.03	36.14 ± 0.02	42.94 ± 0.04	15.28 ± 0.02
Enhancement	1264 ∈ [854, 2430]	1094 ± 202	318 ± 22	138 ± 4	604 ± 11
P_{enh} (%)	0.10 ∈ [0.071, 0.20]	0.091 ± 0.017	0.026 ± 0.002	0.011 ± 0.0004	0.050 ± 0.0009
Δ_{DNP} (MHz)	14	17	30	20	52
D (10^{-14} cm^2/s)	0.67	2.06	3.26	4.62	6.53
L (nm)	3.87	11.09	10.86	14.08	9.99

No. DE-AC02-05CH11231. The authors thank Dr. Ashok Ajoy for helpful discussions and Dr. Melanie Drake and Prof. Jeffrey Reimer for providing the natural abundance sample. This study was made possible by the help of Joseph Tabeling at Applied Diamond, Inc./Delaware Diamond Knives for the custom synthesis of the samples used in this study.

APPENDIX: MATERIALS AND METHODS

^{13}C-enriched diamonds were grown by chemical vapor deposition (Applied Diamond, Inc.) using ^{13}C enrichments of methane with 600-ppm nitrogen as a precursor. ^{13}C concentrations of 10%, 25%, 50%, and 100% ^{13}C were used. These samples were compared to a sample grown by high-pressure high-temperature (HPHT) diamond synthesis (Sumitomo Electric Industries, Inc.) with a substitutional nitrogen concentration of approximately 200 ppm and ^{13}C concentration of 1.1% (natural abundance). All samples were irradiated with 1-MeV electrons at a fluence of 10^{18} cm^{-2} (Prism Gem LLC) and annealed at 800 °C for 2 h to produce an NV$^-$ concentration of 1–10 ppm. Optically detected magnetic resonance (ODMR) and DNP were performed in a purpose-built

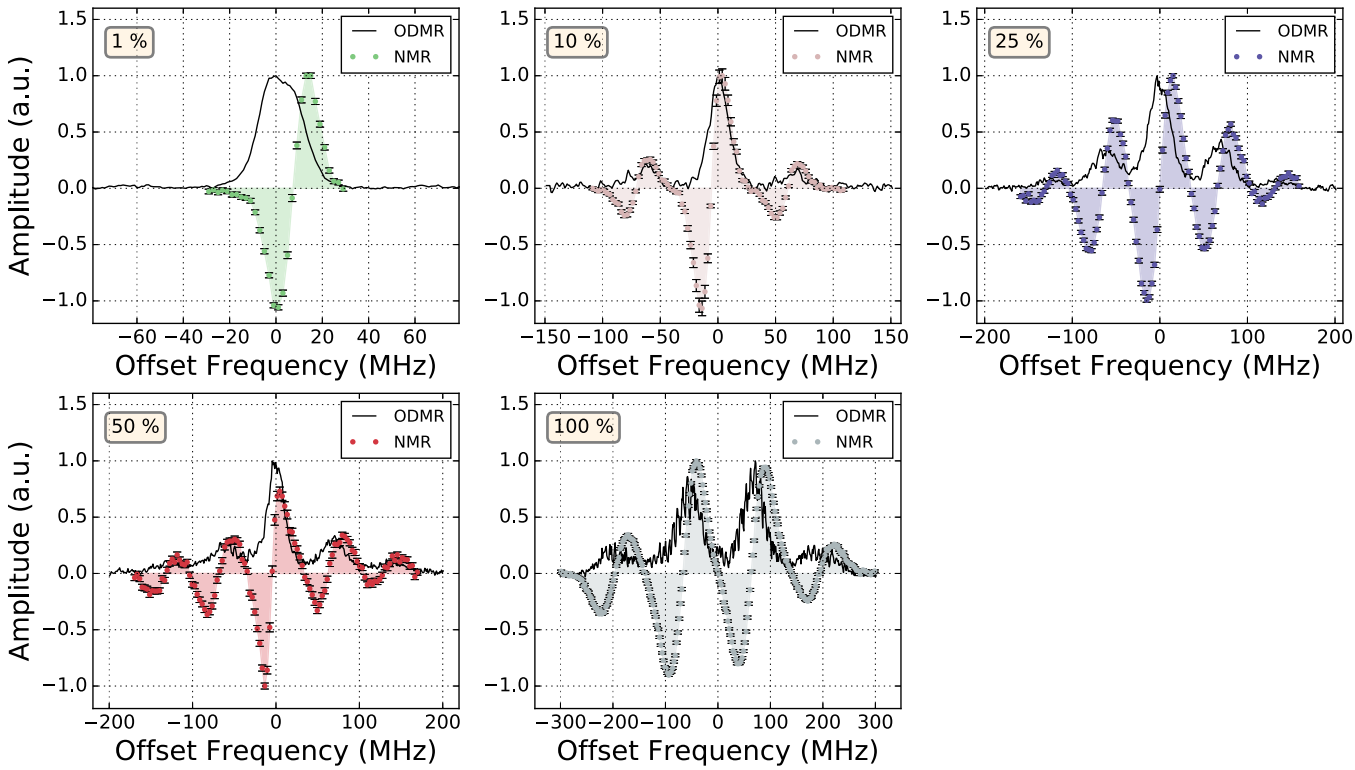

FIG. 3. DNP spectra of the various diamond samples. Normalized hyperpolarized ^{13}C NMR signal as a function of offset microwave frequency for each sample. The normalized ODMR data for each sample are given to show the corresponding high-frequency transition of the NV$^-$ ESR spectrum. cw-DNP experiments are performed at 472.1–473.0 mT, thus the microwave frequency is centered at approximately 16.1 GHz for the various samples with an ^{13}C NMR frequency of approximately 5.06 MHz. It should be noted the signal-to-noise ratio (SNR) of the ODMR spectra shown here differs from that of the ODMR spectra in Fig. 2 because the two were acquired at different microwave amplitudes. The optimum microwave amplitude for DNP measurements is higher than the microwave amplitude for optimized ODMR contrast (see Appendix).

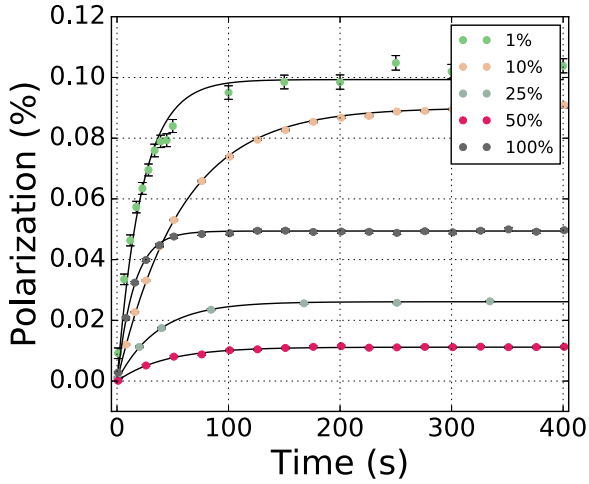

FIG. 4. ^{13}C polarization buildup curves are summarized for all samples involved in the study. Characteristic polarization buildup times T_{DNP} are given in Table I. The sample with 100% ^{13}C enrichment gives the fastest buildup and the largest signal. The maximum polarization as well as the second-fastest buildup rate is observed from the sample with a natural abundance of ^{13}C, which is likely due to it having the highest concentration of NV$^-$ centers [52].

instrument consisting of a custom probe fixed in an electromagnet (GMW Associates, Model 3472-50 with Danfysik 858 power supply). The probe includes a radio-frequency circuit for inductive NMR excitation and detection, a goniometer for two-axis alignment of the defect axis along the magnetic field, a 3-mm wire loop for microwave excitation (Agilent E8257D signal generator), and optical access to the sample (532-nm Coherent Verdi G5 laser). For all DNP experiments, the amplitude of the microwave frequency was set to 10 dBm and amplified with a 3-W amplifier (Mini-Circuits ZVE-3W-183+) before being sent to the 3-mm loop. The NMR circuit includes a 30-turn planar coil of 46 AWG copper wire, with capacitance added to impedance-match the circuit at 5.06 MHz. The NMR components of DNP experiments are carried out with a Magritek Kea^2 console. For ODMR measurements, the microwave amplitude was modulated 100% at 200 Hz from the reference signal of the lock-in amplifier (Stanford Research Systems, SR830) and the fluorescence signal was detected with an avalanched photodiode (APD 410A, Thorlabs). The lock-in amplifier measured the in-phase component of the fluorescence signal at the modulation frequency using a time constant of 30 ms. A spectrum was acquired by stepping through a range of microwave frequency centered on the NV$^-$ ESR, where each step consists of changing the microwave frequency by one step, waiting 50 ms, and measuring the ODMR signal from the lock-in. These spectra were used to characterize the samples, align the defect axis along the magnetic field, and set the strength of the magnetic field as measured by the ensemble of NV$^-$ defects for DNP experiments.

DNP experiments were carried out at 472.2 mT. A schematic of the DNP experiment is shown in Fig. 1. A 532-nm laser with a beam diameter of approximately 5 mm is set to an output power of 1 W/cm^2 and applied continuously throughout experiments. The laser beam is kept large to irradiate the full surface of the diamond. A set of 90° pulses are used to destroy thermal ^{13}C polarization before waiting a time t_{rec} for ^{13}C polarization to build as a result of DNP processes. The microwave frequency is set to f_{MW} and applied continuously for the duration of t_{rec}. A simple 90° pulse-acquire experiment is then used to determine the ^{13}C NMR signal. This is repeated for a range of f_{MW} centered on the NV$^-$ ESR to acquire the DNP spectrum of ^{13}C NMR signal as a function of microwave frequency f_{MW}. The ^{13}C NMR signal was compared by fitting the free induction decay (FID) at $f_{\mathrm{MW},i}$ to the FID of the signal with maximum enhancement by a scaling factor. All data are reported with error bars giving 95% confidence intervals for the scaling factors, taken from the standard deviation of the parameter estimates of the fit. All NMR raw data were acquired with PROSPA (software supplied with the Kea^2 spectrometer) and exported for processing in PYTHON with MATPLOTLIB [53], SCIPY, and NUMPY [54,55] packages [52].

Photoluminescence (PL) experiments [52] were carried out with a home-built confocal microscope to gain a qualitative understanding of the defect content in each of the samples. The confocal microscope involves a 532-nm laser (Opto Engine LLC, MGL-III-532-200mW) directed to the sample through a microscope objective with numerical aperture NA = 0.4 (Nikon M Plan 20 ELWD). From this NA we estimate an excitation volume of 1.9×10^5 μm^3. The objective is also used to collect the fluorescence and direct it through a dichroic mirror to a spectrometer (Mightex HRS-BD1-025). The emissions of the samples were collected using an approximate optical excitation power of 2.5 kW/cm^2. We use the minimum optical power required to detect the emission spectra with the Mightex spectrometer in order to suppress any changes in the emission spectra due to charge-state conversion between NV$^-$ and NV^0. Emission spectra were collected from 16 random points in each of the samples. Each spectrum was averaged 256 times with an exposure time of 100 ms. The raw data were acquired using the software provided by Mightex for interfacing with the spectrometer, and exported for processing in PYTHON.

[1] W. F. Koehl, B. B. Buckley, F. J. Heremans, G. Calusine, and D. D. Awschalom, Nature (London) **479**, 84 (2011).

[2] M. Widmann, S.-Y. Lee, T. Rendler, N. T. Son, H. Fedder, S. Paik, L.-P. Yang, N. Zhao, S. Yang, I. Booker *et al.*, Nat. Mater. **14**, 164 (2015).

[3] M. W. Doherty, N. B. Manson, P. Delaney, F. Jelezko, J. Wrachtrup, and L. C. L. Hollenberg, Phys. Rep. **528**, 1 (2013).

[4] N. Manson and R. McMurtrie, J. Lumin. **127**, 98 (2007).

[5] G. Balasubramanian, P. Neumann, D. Twitchen, M. Markham, R. Kolesov, N. Mizuochi, J. Isoya, J. Achard, J. Beck, J. Tissler *et al.*, Nat. Mater. **8**, 383 (2009).

[6] D. J. Christle, A. L. Falk, P. Andrich, P. V. Klimov, J. U. Hassan, N. T. Son, E. Janzén, T. Ohshima, and D. D. Awschalom, Nat. Mater. **14**, 160 (2015).

[7] M. W. Doherty, N. B. Manson, P. Delaney, and L. C. L. Hollenberg, New J. Phys. **13**, 025019 (2011).

[8] N. Yao, L. Jiang, A. Gorshkov, P. Maurer, G. Giedke, J. Cirac, and M. Lukin, Nat. Commun. **3**, 800 (2012).

[9] B. Hensen, H. Bernien, A. E. Dréau, A. Reiserer, N. Kalb, M. S. Blok, J. Ruitenberg, R. F. Vermeulen, R. N. Schouten, C. Abellán *et al.*, Nature (London) **526**, 682 (2015).

[10] P. V. Klimov, A. L. Falk, D. J. Christle, V. V. Dobrovitski, and D. D. Awschalom, Sci. Adv. **1**, e1501015 (2015).

[11] J. Cai, A. Retzker, F. Jelezko, and M. B. Plenio, Nat. Phys. **9**, 168 (2013).

[12] A. Ajoy and P. Cappellaro, Phys. Rev. Lett. **110**, 220503 (2013).

[13] J. M. Taylor, P. Cappellaro, L. Childress, L. Jiang, D. Budker, P. R. Hemmer, A. Yacoby, R. Walsworth, and M. D. Lukin, Nat. Phys. **4**, 810 (2008).

[14] J. R. Maze, P. L. Stanwix, J. S. Hodges, S. Hong, J. M. Taylor, P. Cappellaro, L. Jiang, A. Zibrov, A. Yacoby, R. Walsworth *et al.*, Nature (London) **455**, 644 (2008).

[15] G. Balasubramanian, I.-Y. Chan, R. Kolesov, M. Al-Hmoud, C. Shin, C. Kim, A. Wojcik, P. R. Hemmer, A. Krüger, F. Jelezko *et al.*, Nature (London) **445**, 648 (2008).

[16] N. Bar-Gill, L. Pham, C. Belthangady, D. Le Sage, P. Cappellaro, J. Maze, M. Lukin, A. Yacoby, and R. Walsworth, Nat. Commun. **3**, 858 (2012).

[17] M. V. G. Dutt, L. Childress, L. Jiang, E. Togan, J. Maze, F. Jelezko, A. S. Zibrov, P. R. Hemmer, and M. D. Lukin, Science **316**, 1312 (2007).

[18] P. Neumann, R. Kolesov, B. Naydenov, J. Beck, F. Rempp, M. Steiner, V. Jacques, G. Balasubramanian, M. L. Markham, D. J. Twitchen *et al.*, Nat. Phys. **6**, 249 (2010).

[19] A. Reiserer, N. Kalb, M. S. Blok, K. J. M. van Bemmelen, T. H. Taminiau, R. Hanson, D. J. Twitchen, and M. Markham, Phys. Rev. X **6**, 021040 (2016).

[20] A. Laraoui, F. Dolde, C. Burk, F. Reinhard, J. Wrachtrup, and C. A. Meriles, Nat. Commun. **4**, 1651 (2013).

[21] T. Rosskopf, J. Zopes, J. M. Boss, and C. L. Degen, npj Quantum Inf. **3**, 33 (2017).

[22] A. Ajoy, Y. X. Liu, and P. Cappellaro, arXiv:1611.04691.

[23] N. Khaneja, Phys. Rev. A **76**, 032326 (2007).

[24] T. W. Borneman, C. E. Granade, and D. G. Cory, Phys. Rev. Lett. **108**, 140502 (2012).

[25] N. Kalb, A. A. Reiserer, P. C. Humphreys, J. J. Bakermans, S. J. Kamerling, N. H. Nickerson, S. C. Benjamin, D. J. Twitchen, M. Markham, and R. Hanson, Science **356**, 928 (2017).

[26] H. Weimer, N. Y. Yao, and M. D. Lukin, Phys. Rev. Lett. **110**, 067601 (2013).

[27] A. Ajoy and P. Cappellaro, Phys. Rev. B **87**, 064303 (2013).

[28] N. Y. Yao, C. R. Laumann, S. Gopalakrishnan, M. Knap, M. Müller, E. A. Demler, and M. D. Lukin, Phys. Rev. Lett. **113**, 243002 (2014).

[29] R. Nandkishore and D. A. Huse, Annu. Rev. Condens. Matter Phys. **6**, 15 (2015).

[30] V. Khemani, A. Lazarides, R. Moessner, and S. L. Sondhi, Phys. Rev. Lett. **116**, 250401 (2016).

[31] D. V. Else and C. Nayak, Phys. Rev. B **93**, 201103 (2016).

[32] S. Choi, J. Choi, R. Landig, G. Kucsko, H. Zhou, J. Isoya, F. Jelezko, S. Onoda, H. Sumiya, V. Khemani *et al.*, Nature (London) **543**, 221 (2017).

[33] A. L. Falk, P. V. Klimov, V. Ivády, K. Szász, D. J. Christle, W. F. Koehl, Á. Gali, and D. D. Awschalom, Phys. Rev. Lett. **114**, 247603 (2015).

[34] E. Scott, M. Drake, and J. A. Reimer, J. Magn. Reson. **264**, 154 (2016).

[35] T. Wenckebach, *Essentials of Dynamic Nuclear Polarization* (Spindrift, Burgh-Haamstede, The Netherlands, 2016).

[36] P. London, J. Scheuer, J.-M. Cai, I. Schwarz, A. Retzker, M. Plenio, M. Katagiri, T. Teraji, S. Koizumi, J. Isoya *et al.*, Phys. Rev. Lett. **111**, 067601 (2013).

[37] R. Fischer, A. Jarmola, P. Kehayias, and D. Budker, Phys. Rev. B **87**, 125207 (2013).

[38] G. A. Álvarez, C. O. Bretschneider, R. Fischer, P. London, H. Kanda, S. Onoda, J. Isoya, D. Gershoni, and L. Frydman, Nat. Commun. **6**, 8456 (2015).

[39] J. P. King, P. J. Coles, and J. A. Reimer, Phys. Rev. B **81**, 073201 (2010).

[40] J. Scheuer, I. Schwartz, Q. Chen, D. Schulze-Sünninghausen, P. Carl, P. Höfer, A. Retzker, H. Sumiya, J. Isoya, B. Luy *et al.*, New J. Phys. **18**, 013040 (2016).

[41] Q. Chen, I. Schwarz, F. Jelezko, A. Retzker, and M. B. Plenio, Phys. Rev. B **92**, 184420 (2015).

[42] Q. Chen, I. Schwarz, F. Jelezko, A. Retzker, and M. B. Plenio, Phys. Rev. B **93**, 060408(R) (2016).

[43] J. P. King, K. Jeong, C. C. Vassiliou, C. S. Shin, R. H. Page, C. E. Avalos, H.-j. Wang, and A. Pines, Nat. Commun. **6**, 8965 (2015).

[44] B. L. Green, B. G. Breeze, G. J. Rees, J. V. Hanna, J.-P. Chou, V. Ivády, A. Gali, and M. E. Newton, Phys. Rev. B **96**, 054101 (2017).

[45] E. Rej, T. Gaebel, T. Boele, D. E. J. Waddington, and D. J. Reilly, Nat. Commun. **6**, 8459 (2015).

[46] A. J. Parker, H.-J. Wang, Y. Li, A. Pines, and J. P. King, arXiv:1506.05484.

[47] J. H. Shim, B. Nowak, I. Niemeyer, J. Zhang, F. D. Brandao, and D. Suter, arXiv:1307.0257.

[48] D. Shimon, Y. Hovav, A. Feintuch, D. Goldfarb, and S. Vega, Phys. Chem. Chem. Phys. **14**, 5729 (2012).

[49] C. J. Terblanche, E. C. Reynhardt, and J. A. van Wyk, Solid State Nucl. Magn. Reson. **20**, 1 (2001).

[50] H. Hayashi, T. Itahashi, K. M. Itoh, L. S. Vlasenko, and M. P. Vlasenko, Phys. Rev. B **80**, 045201 (2009).

[51] C. Kittel and E. Abrahams, Phys. Rev. **90**, 238 (1953).

[52] See Supplemental Material at http://link.aps.org/supplemental/10.1103/PhysRevB.100.041203 for sample characterization including relaxation times, for a description of the calibration against thermal equilibrium, for a discussion of defect concentration, for further discussion of the data analysis, and for a description of the photoluminescence experiments.

[53] J. D. Hunter, Comput. Sci. Eng. **9**, 90 (2007).

[54] S. van der Walt, S. C. Colbert, and G. Varoquaux, Comput. Sci. Eng. **13**, 22 (2011).

[55] E. Jones, T. Oliphant, P. Peterson *et al.*, SciPy: Open source scientific tools for PYTHON (2001), URL: http://www.scipy.org/.